Increased fluid flow activity in shallow sediments at the 3-km long Hugin Fracture in the Central North Sea

A. Lichtschlag[1*], M. Cevatoglu[2+], D.P. Connelly[1], R.H. James[1, 2] and J.M. Bull[2]

[1] National Oceanography Centre, University of Southampton Waterfront Campus, Southampton, UK.

[2] Ocean and Earth Science, University of Southampton, National Oceanography Centre Southampton, Southampton, UK.

*Corresponding author: Anna Lichtschlag, a.lichtschlag@noc.ac.uk

+Current address: Fugro Sial Geosciences Consulting and Engineering, Istanbul, Turkey

Key Points:

- *We provide evidence for fluid flow within shallow sediments at the Hugin Fracture in the Central North Sea*
- *Shallow sediment porewaters have two different sources*
- *Seismic amplitude anomalies show a bright spot in the shallow sediments that is indicative of the presence of gas-rich fluids at a fault bend*

1

Abstract

The North Sea hosts a wide variety of seafloor seeps that may be important for transfer of chemical species, such as methane, from the Earth's interior to its exterior. Here we provide geochemical and geophysical evidence for fluid flow within shallow sediments at the recently discovered, 3-km long Hugin Fracture in the Central North Sea. Although venting of gas bubbles was not observed, concentrations of dissolved methane were significantly elevated (up to six-times background values) in the water column at various locations above the fracture, and microbial mats that form in the presence of methane were observed at the seafloor. Seismic amplitude anomalies revealed a bright spot at a fault bend that may be the source of the water column methane. Sediment porewaters recovered in close proximity to the Hugin Fracture indicate the presence of fluids from two different shallow (<500m) sources: (i) a reduced fluid characterized by elevated methane concentrations and/or high levels of dissolved sulfide (up to 6 mmol L^{-1}), and (ii) a low-chlorinity fluid (Cl ~305 mmol L^{-1}) that has low levels of dissolved methane and/or sulfide. The area of the seafloor affected by the presence of methane-enriched fluids is similar to the footprint of seepage from other morphological features in the North Sea.

1 Introduction

Methane-rich fluids are present worldwide in continental margin sediments (Judd and Hovland 2009) and sedimentary methane is a potential hazard that can trigger slope instabilities (Vanneste et al., 2014) and cause accidental blow-outs during hydrocarbon exploration drilling. Any methane that reaches the atmosphere will also act as a potent greenhouse gas, accelerating global warming (McGinnis et al., 2006, Skarke et al., 2015). It is estimated that geological sources, including marine methane release, contribute ~45 Tg yr^{-1} of methane to the atmosphere (Etiope et al. 2008; Kvenvolden and Rogers, 2005), which is <10% of global methane atmospheric emissions (Ciais et al., 2014). Recent estimates based on long-term carbon isotope records indicate that methane emission from natural gas, oil and coal production might, however, be much higher than previously suggested (Schwietzke et al., 2016). The importance of the marine contribution to methane emissions is uncertain as monitoring of fluid flow activity remains a challenge and uncertainties exist in understanding of fluid migration pathways, fluid alteration processes and leakage rates. Moreover, new seafloor features with methane-rich fluids in the near-surface sediments are continually being discovered (e.g. Krämer et al., 2017).

There are a number of reliable indicators for the presence of fluid flow activity and methane-rich fluids in near-surface sediments. These include geomorphological indicators such as the presence of pockmarks and mud volcanoes (Chen et al., 2015; Dupré et al., 2014; Holvand and Sommerville, 1985; Pierre et al., 2014) that are interpreted to be caused by sustained gas seepage from deeper hydrocarbon reservoirs that are in hydraulic connection with the sediment overburden (Karstens and Berndt, 2015; Nicoll et al., 2012; Heggland, 1997). These gases and fluids migrate from depth through buried faults and glacially-derived tunnel valleys that can reach the seabed and transfer material into the water column and ultimately to the atmosphere (Cartwright, 2011; Cartwright, 1994; Cavanagh and Haszeldine, 2014; Nicoll, 2012; Schroot et al., 2005; Wiprut and Zoback, 2000). The presence of fluid flow within shallow sediments can also be inferred from seismic reflection data by the presence of characteristic variations in the amplitude/reflection coefficient of the seismic signal (Cevatoglu et al., 2015; Tóth et al., 2014; Wiggins et al., 2015), and from steep gradients in porewater chemistry (e.g. Holvand et al., 2012). The chemical composition of the porewaters is strongly dependent on their origin, their migration and, as they are often highly reactive, their chemical transformation during transport. Finally, the presence of white microbial mats at the seafloor formed by giant filamentous sulfide oxidizing bacteria is often used as a proxy for the presence of reduced, methane-containing

fluids in the shallow subsurface (e.g. Hovland and Svensen, 2006; Hovland et al. 2012). These microbial mats live on the sulfide produced by the microbial turnover of methane with sulfate deeper in the sediment (anaerobic oxidation of methane: $CH_4 + SO_4^{2-} \rightarrow HS^- + HCO_3^- + H_2O$, (Eq. 1), Boetius et al. 2000) and can be detected by video-imaging and biogeochemical analyses of sediments. Methane oxidation can also be associated with the precipitation of methane-derived authigenic carbonates that accumulate at the seafloor or in the sediments (Aloisi et al., 2002). However, the presence of authigenic carbonates and specific chemosynthetic habitats largely depends on the rate of the fluid flow and they are not always visible at the sediment surface (Lichtschlag et al., 2010). If fluid flow rates are low or are variable with time (Grünke et al., 2011), near-surface seabed fluid flow can be hard to detect, but the fluids can still be an important source of reduced substances into surface sediments and a threat to drilling operations (e.g., Judd and Hovland, 2009). At high flow rates, the microbial filter that consumes methane within the sediments is not always effective. Thus release of methane to the water column is common, especially in shallow continental margins such as the North Sea, where the water column is frequently mixed by storms and methane emissions from the seabed can reach the atmosphere (Sommer et al., 2015; von Deimling et al., 2011).

The Central North Sea is a globally important hydrocarbon province. Numerous fluid flow structures exist in the shallow sediment overburden, including bright spots and seismic chimneys. Surface expressions of the presence of near-surface fluid flow activity include pockmarks and macro-seeps, such as the Tommeliten, the Scanner pockmark and the Gullfaks seep areas in the North Sea (Hovland et al., 2012). A new structure (Figure 1), the 3-km long Hugin Fracture, was discovered in 2011 in the Southern Viking Graben (Central North Sea, Norwegian Sector, block 16/4) and analysis of sub-bottom profiler data revealed the presence of bright spots that are interpreted to represent gas accumulations within the shallow strata (Landschulze and Pedersen, 2013; Landschulze et al., 2014; Pedersen et al., 2013). To determine the chemical composition and sources of material to the shallow sub-surface sediments, we conducted a multidisciplinary study of the shallow sediments in the vicinity of the Hugin Fracture. Fluid flow activity was monitored using geophysical tools mounted on an Autonomous Underwater Vehicle (AUV), shipboard multibeam bathymetry surveys and seabed video photography with a towed underwater vehicle. The composition of porewaters in the shallow subsurface sediments was verified by geochemical analyses of sediment cores. These data

indicate that the Hugin Fracture acts as conduit for fluid exchange between the subsurface sediments and the seafloor, and provides a source of methane to the overlying water column.

2 Geological setting and study area

The Hugin Fracture is located in the Southern Viking Graben (Utsira High) in the Central North Sea (Figure 1a). The Southern Viking Graben contains hydrocarbon-rich Paleocene sediments (Heimdal Formation) that are charged by Jurassic source rocks (Justwan and Dahl, 2005). The hydrocarbon-bearing units are overlain by the Miocene-Pliocene Utsira Formation. The uppermost Quaternary sediments are significantly disturbed by Pleistocene glaciations that led to episodic erosion and infill of the basin, with the formation of glacio-morphological features, including subglacial tunnel valleys and ploughmarks (Sejrup et al., 2000; Lonergan et al., 2006; Dowdeswell and Ottesen, 2013; Praeg, 2003).

Since 1996 the Utsira Formation has been used to store CO_2 that is a natural by-product of the gas extraction at the nearby Sleipner production site. The depth of the top of the Utsira Formation differs regionally from 550-1500 m below seafloor (Chadwick et al., 2004). The Utsira Formation is capped by the low permeability sands and mudstones of the Nordland Shales (Northland Group), which are assumed to act as effective seal for fluid migration from below (Harrington et al., 2009). Above that seal, shallow gas pockets can be present in the Northland Group sediments and seismic chimneys imply hydraulic connectivity between the strata (Karstens and Berndt, 2015).

3 Methods

A multidisciplinary study of the Hugin Fracture was carried out in 2012 during RRS *James Cook* cruise JC77. The main target areas for the study were the Hugin Fracture and its surrounding area, mainly south and east of the Hugin Fracture, but also including the abandoned hydrocarbon exploration well 16/4-2 (Figure 1). Detailed information on all sampling stations in the working area is given in Table S1.

3.1 Visual seafloor observations

High-quality visual imagery of the seabed was acquired with a 5 Mega-pixel digital downward looking color camera mounted on the AUV “Autosub 6000” with 60,000-70,000 image frames collected per deployment. More targeted observations were carried out with

HyBIS, a survey and sampling robotic underwater vehicle. The navigation of HyBIS was provided using the ship's Sonardyne USBL tracking system with a mini-transponder beacon on the HyBIS vehicle.

3.2 High-resolution 2D seismic reflection

High-resolution 2D seismic reflection data (Chirp) were acquired using an Edgetech 2200-M Modular Sonar System, mounted on the AUV. The source sweep used during seismic data acquisition was a high frequency Chirp sweep, developed by Gutowski et al. (2002) that oscillated between 2-13 kHz for 32 ms, with sine squared 8th envelope. The Chirp data were sampled at 43.4 kHz. The maximum penetration depth into the sediment was around 5 m (for V_p=1500 m/s) throughout the surveys. Due to the high quality of the collected data, only simple Chirp data processing was necessary: Correlation of the raw data with the source sweep, Ormsby band-pass filtering (1000-2000-10000-12000 Hz), minimum phase predictive deconvolution, trace mixing (3 traces), true amplitude recovery, trace muting, and instantaneous amplitude correction (Quinn et al., 1998; Cevatoglu et al., 2015). The processed Chirp data were then corrected for depth using the shipboard multibeam bathymetry data (EM710).

Root Mean Square (RMS) seismic amplitudes (A_{RMS}) were calculated for Chirp seismic reflection data using Eq. 2:

$$A_{RMS} = \sqrt{\frac{A_1^2 + A_2^2 + \cdots + A_m^2}{m}} \qquad (Eq. 2)$$

where *m* is the total number of samples within the selected time window. After the extraction of RMS seismic amplitude along trace, these values were gridded and RMS seismic amplitude maps produced. The limited electrical power available to drive the single transducer on the AUV, together with the coarse grain-size of the near-surface sediments, meant that the Chirp signal only penetrated the top 5 m of the sediment.

Side-scan sonar data were acquired with an Edgetech 2200-M Modular Sonar mounted on the AUV. The side-scan sonar operated at 410 kHz, with one-way beam being 0.3°, and 200 m swath. Survey speed was about 2.8 knots and the ping rate was approximately 0.3 m.

Following each AUV deployment, amplitude corrections were applied to the raw data, followed by the production of side-scan mosaics. The side-scan mosaics were processed at 0.5 m.

3.3 Geochemistry

3.3.1 Water column sampling and analyses

Water column methane concentrations were determined in water samples collected in Niskin bottles attached to a Conductivity, Temperature, Depth (CTD) rosette. A total of 63 CTD hydrocast transects were performed in the study area and samples for CH_4 analysis were collected at ~6, 8, 13 and 20 m above the seafloor and at 5 m below the seawater-air interface during each CTD deployment. To avoid contact with the atmosphere and the formation of bubbles, the seawater was collected in 500 mL blood bags using silicon tubing. Extraction of the methane from the seawater was done using the headspace method of Swinnerton et al. (1976); 60 mL of nitrogen headspace was introduced to all blood bags and the bags were allowed to equilibrate at 24°C for at least 2 hours. Methane concentration was determined by gas chromatography with flame ionization detector (GC-FID); to this end 20 mL of headspace gas was injected through a short desiccating column into the GC-FID and methane concentrations were determined from the area of peaks consistently produced at a retention time of 1.68 minutes. Peak heights were calibrated using 3 standards (a blank of pure N_2, 10 ppm CH_4 and 20 ppm CH_4) and an atmospheric measurement. Every 10 samples the 10 ppm CH_4 standard was re-run to check for instrument drift. The accuracy and precision of this technique is better than ±1%.

3.3.2 Sediment coring and geochemical analyses of porewaters and sediments

Sediment cores of up to 3.8 m length were collected using a vibrocorer at 12 stations at the Hugin Fracture, the abandoned well 16/4-2 and in the surrounding area (Table S1), at water depths between 83 to 99 m. Positions for sediment cores were selected with the help of HyBIS and AUV images. Comparison of the actual core length with the core penetration depth recorded by an echosounder mounted on the vibrocorer showed that loss of surface sediments during core recovery was minimal.

Immediately after retrieval, the vibrocores (VCs) were sectioned into 0.5 m intervals, capped and transported into a controlled temperature room cooled to in situ temperature (~7° C). Here, holes for sub-sampling were drilled into the plastic liners and taped to limit oxygen

contamination. For sub-sampling sediments and porewaters under an oxygen-free atmosphere the sections were transferred into an anaerobic chamber filled with nitrogen.

Porewater was extracted from sediments directly with Rhizons (Rhizon CSS: length 5 cm, pore diameter 0.2 μm; Rhizosphere Research Products, Wageningen, Netherlands) inserted through the pre-drilled holes in the VC liners and connected to a syringe to which a small under pressure was applied. For some of the dry sandy sediments outside the Hugin Fracture, sediment samples were removed using plastic syringes through larger holes in the VC liners, transferred into centrifuge vials inside the nitrogen-filled anaerobic chamber and centrifuged for 6-10 minutes at 10,000 rpm for compaction of the sediments. Afterwards, porewater was extracted from these sediments inside the anaerobic chamber with Rhizons inserted into the vials prior to centrifugation.

Aliquots of 2 mL of porewater were taken for dissolved inorganic carbon (DIC) analyses and for analysis of the carbon isotopic composition of the DIC ($\delta^{13}C_{DIC}$) and poisoned with mercuric chloride (5 μL) to prevent continued microbial turnover. A further 2.5 mL of the porewaters were acidified with 6 μL of concentrated suprapure HNO_3 for analyses of cations. 1-2 mL of the porewater were sub-sampled in the anaerobic chamber and fixed with zinc acetate for H_2S analyses and sub-samples were also taken for analysis of sulfate and chloride; these samples were also fixed with zinc acetate if sulfide was present. Total Alkalinity (TA) was measured on board immediately after porewater sampling, by titration against 0.0005 mol L^{-1} HCl using a mixture of methyl red and methylene blue as an indicator. Analyses were calibrated against IAPSO seawater (certified by the International Association for the Physical Sciences of the Oceans) and the reproducibility of the analyses was better than ±1%. Any remaining porewater was frozen at -20 °C for nutrient analyses.

To determine the methane concentration in the sediments 3 cm^3 of sediment was sampled using a cut-off syringe, transferred to a headspace vial containing 5 mL of 1 mol L^{-1} NaOH and crimp-sealed. Methane concentration was determined on board on 10 mL of the headspace by gas chromatography as described above. To determine the porosity of the sediment 5 cm^3 sub-samples were taken and stored in plastic containers at 4 °C. The porosity of the sediments was determined by the mass difference between wet and dried samples.

Back onshore, cation (B, Ba, Ca, Fe, Na, Li, Mg, Sr, Rb) concentrations were measured by inductively coupled plasma optical emission spectrometry (ICP-OES; Perkin-Elmer Optima 4300 DV) after diluting the samples by a factor of 50 with 3% thermally distilled HNO_3. Standards were prepared from single element standard solutions that covered the range of sample concentrations. Measured concentrations of a certified reference material seawater standard (CRM-SW; High Purity Standards) were within ±5% of the certified values for all elements. Anions were measured by ion chromatography (Dionex ICS 2500) with 9 mmol L^{-1} $NaCO_3$ as the eluent. Repeat analysis of IAPSO seawater and of single anion standards indicates that the reproducibility of the Cl and SO_4 analyses was better than ±1%. DIC was measured using an Apollo SciTech DIC analyzer (AS-C3), using a LI-COR CO_2/H_2O (LI-7000) infrared analyzer to detect CO_2 released from the sample after acidifying with 10% H_3PO_4. The carbon isotopic composition of the DIC ($\delta^{13}C_{DIC}$) was determined using a multiflow preparation system coupled to an Isoprime continuous flow mass spectrometer at Royal Holloway University of London. Measurements were made by injecting 0.5 mL of water into vials containing orthophosphoric acid that had been flushed with helium and equilibrating the acid and water for 4 hours at 40 °C (Mattey et al., 2008). $\delta^{13}C_{DIC}$ values were normalized to the VPDB (Vienna Pee Dee Belemnite) scale via a calibrated sodium bicarbonate internal standard and the standard deviation of 2 replicate measurements was less than ±0.3‰. Total dissolved sulphide concentrations ($H_2S + HS^- + S^{2-}$) were determined using the diamine method (Cline, 1969). Nutrient concentrations (phosphate, silicate, NOx, ammonium) were measured with a QuAAtro nutrient analyzer. $^{87}Sr/^{86}Sr$ isotope ratios in the porewaters were determined by thermal ionization mass spectrometry (TIMS). For the Sr isotope analysis a sub-sample of the porewater containing approximately 1 μg of Sr was loaded onto a column containing 50 μL of Sr-Spec resin. The sample matrix was eluted with 3 mol L^{-1} HNO_3, and the Sr fraction was then collected in MilliQ water. The purified Sr sample was dried and loaded onto a single Ta filament using a Ta activator solution and $^{87}Sr/^{86}Sr$ ratios were measured with a Thermo Fisher Triton Plus TIMS using a static routine with amplifier rotation with a ^{88}Sr beam intensity of 2V for 300 ratios. Results were normalized to a $^{86}Sr/^{88}Sr$ ratio of 0.1194 using an exponential correction. Analyses of the Sr isotope standard NBS987 give $^{87}Sr/^{86}Sr = 0.710247 \pm 0.000024$ (2 SD; n = 106). The standard error of duplicate measurement was less than 17 ppm.

Sediment cores were split at the British Ocean Sediment Core Research Facility (BOSCORF) in Southampton, UK, and the archive half of each core was logged for magnetic

susceptibility with a XYZ Multi-Sensor Core Logger (Geotek) at 1 cm intervals. Relative abundances of elements were measured on the archive core half by X-ray fluorescence (ITRAX core-scanning X-ray fluorescence system, Cox Analytical; Croudace et al. 2006). The instrument was operated at a voltage of 30 kV and a current of 50 mA, with a count time of 30 s and at 1000 μm sample resolution. Element abundances are normalized to kcps (kilo-counts per second) and a running average of 0.5 cm was applied to the results.

3.3.3 Formation water sampling

Formation waters were sampled from the Ustira Formation. Samples were taken at wellbore 15/9-F-07 (58° 26' 29.87" N, 1° 53' 14.86" E, water depth 91 m) and 15/9-F-09 (58° 26' 29.74" N, 1° 53' 15" E, water depth 91 m) in 2011 and 2014. The wellbore penetrates the Utsira sands between ~880 – 1065 m below seafloor. pH and temperature were measured immediately after fluid recovery and the chemical composition of the fluids was determined in the same way as the porewater samples.

4 Results

4.1 Side scan, multibeam and seafloor observations

Side-scan sonar and optical imagery, together with sediment samples show that the seabed around the Hugin Fracture comprises sandy sediments, corresponding to low side-scan backscatter regions, and shell hashes that have higher backscatter (Figures 1, 2). The surface trace of the Hugin Fracture imaged on a side-scan sonar mosaic is around 1.6 km long, up to 5 m wide, has a very complex surface geometry (Figure 1 b-d), and appears as a sharp discontinuity on the seabed. The side-scan imagery reveals that the Hugin Fracture is made of two major fault segments, A and B, which are orientated NE-SW in an en echelon configuration, separated by a fault bend orientated NW-SE. The more easterly fault segment, Segment A, comprises zig-zagging, sub-parallel fractures, oriented NE-SW, and imaged over approximately 260 m (Figure 1d). These subsidiary fractures are connected to each other via small fault bends in a NW-SE direction. Segment B is around 1.2 km long and fairly linear, oriented NE-SW; however smaller fault bends and step overs oriented NW-SE are also found along strike, connecting zig-zagging more minor fractures. Unlike Segment A, Segment B is more discontinuous towards its end, suggesting burial by mobile surficial sediments (Figure 1d). In places (for example at the western end of Segment B), splaying of the fault segment is seen with two surface traces. Although the fault traces look relatively fresh, there is little change in depth along or across the

Hugin Fracture (varying between 93-94 m depth), although north of the main fault bend the seabed is slightly depressed.

Black sediments, with and without white mats formed by sulfide oxidizing bacteria, are evidence for the presence of methane-rich fluids in the near-surface sediments along the Hugin Fracture and in the vicinity of abandoned well 16/4-2 (Figure 2). At well 16/4-2, video images collected using the HyBIS remotely operated vehicle show bubbles venting from the sediment into the water column, and large patches with microbial mats cover the sediment. Evidence for the presence of reduced, methane-enriched fluids in near-surface sediments all along the Hugin Fracture is provided by the continuous presence of microbial mats and dark sediment patches. However, no seabed authigenic carbonates or bubble streams were detected along the fracture during our survey. Black spots and microbial mats extend about 10 m perpendicular to the fracture. Apart from along the Hugin Fracture and at well 16/4-2, there is no other visual evidence of fluid flow activity or bubble plumes within our 25 km^2 survey area.

4.2. Seismic Reflection Amplitude Mapping

On Chirp seismic reflection data, the Hugin Fracture appears as a sharp, sub-vertical discontinuity, traced down to approximately 5 m below the seabed (Figure 3), and is associated with sub-meter scale vertical displacement. Further analysis of Chirp data reveals high amplitude seismic reflection anomalies within the overburden, along the Hugin Fracture and at the abandoned well 16/4-2, concentrated at around 1 m depth below the seabed. However, gas flares are only observed at the abandoned well site from Chirp data, consistent with overburden seismic anomalies detected at this location, whereas no indication of fluid venting at the seafloor is found at the Hugin Fracture from the Chirp dataset.

A Root Mean Square (RMS) seismic amplitude map, superimposed on the side-scan data, illustrates seismic amplitudes to ca. 2.5 m below the seabed from the Chirp data (Figure 4). The eastern side of the Hugin Fracture area, including the Hugin Fracture, has been found to have slightly higher seismic amplitudes compared to the western side of the survey area. The largest seismic amplitude anomalies are restricted to the main fault bend along the Hugin Fracture and to the abandoned well site. These very localized seismic amplitude anomalies, especially along the Hugin Fracture, likely indicate a patchy fluid flow pattern along this seabed discontinuity, rather than a continuous fluid flow activity throughout the fracture (Figure 2).

294

295 **4.3. Geochemistry**

296 **4.3.1 Methane distribution in the water column**

297 Figure 5 shows the distribution of dissolved methane in the water column within the
298 study area. Within 20 m of the seabed of the area to the south of the Hugin Fracture, methane
299 concentrations range between 30 and 930 nmol L^{-1} with an average of 310 ±250 (average ±SD)
300 nmol L^{-1} (Figure 5a). Methane concentrations in the area around the abandoned well, which has
301 a methane release rate of ~4 t CH_4 yr^{-1} (Vielstädte et al., 2015), are 660 ±140 nmol L^{-1} (Figure
302 5b). In the vicinity of the Hugin Fracture methane concentrations are between 1050 and 3160
303 nmol L^{-1} with an average of 1950 ±620 nmol L^{-1} (Figure 5b). This value is far higher than that
304 measured in bottom waters to the south of the Hugin Fracture, and values measured in the
305 vicinity of the abandoned well (which is >2 km from the Hugin Fracture). Although highest
306 methane concentrations are found above Segment A of the Hugin Fracture, high methane
307 concentrations also occur above Segment B at several locations (Figure 5b). In the surface
308 waters methane concentrations are ~20 ±10 nmol L^{-1}.

309

310 **4.3.2 Sediment lithology and geochemistry**

311 Locations of sediment cores taken at the Hugin Fracture are given in Figure 4. The upper
312 3.8 m of the subseabed sediments recovered with the VCs is characterized by three different
313 horizons (Figures 6, S1, S2): (i) a surface layer that usually has a thickness of 5-25 cm and
314 consists of sandy sediments of dark brown colour; (ii) a shelly layer of up to 5-15 cm thickness,
315 which is present in most of the cores; and (iii) a lower layer of sandy sediments that have a
316 uniform appearance. The upper 2 layers are characterized by high Fe and S concentrations that
317 correlate with increases in magnetic susceptibility. High magnetic susceptibility indicates the
318 presence of magnetic Fe-S minerals (Figure 6). These uppermost sediments also show intervals
319 with high Ca concentrations that coincide with the occurrence of bivalve shell debris. The
320 chemical composition of sediments in the lowermost sandy layer is relatively uniform, except for
321 occasional increases in Ca, Fe and S content (e.g. in VC10; Figure 6b) that coincide with the
322 presence of single shells. The porosity of the sediments is 0.37 ±0.03 and is relatively constant
323 both within cores and between cores. No authigenic carbonates were found in the upper 3.8 m of
324 the sediments or at the sediment surface.

325

326 **4.3.2 Porewater geochemistry**

Results of sediment porewater analyses of anions, cations, methane, sulfide, nutrients, DIC, TA and $\delta^{13}C_{DIC}$ are shown in Figure 6. Dissolved sulfide in porewaters was detected in all four cores sampled close to the Hugin Fracture (VC08, VC10, VC14, VC28; Figure 6a-e). Highest concentrations of dissolved sulfide are found in cores VC08 and VC10 (eastern part of Segment B, up to 6.0 mmol L^{-1} and 4.5 mmol L^{-1}, respectively) and lower concentrations were measured in VC14 (up to 0.3 mmol L^{-1}) and VC28, (up to 1.4 mmol L^{-1}). Note that concentrations of dissolved sulfide are very low at the top, and bottom, of these two cores. Low concentrations of dissolved sulfide coincide with increases in solid phase S and Fe and magnetic susceptibility, indicating sulfide removal by iron-sulfide precipitation. In cores sampled further from the Hugin Fracture, sulfide concentrations are below detection limit.

Methane concentrations are elevated in the upper 0.5 m of one core (VC08) with concentrations reaching ~800 µmol L^{-1} at 0.2 m (Figure 6a). In all other cores containing sulfide, methane concentrations are 2 orders of magnitude lower (<6 µmol L^{-1}, Figure 6a-e). The measured maximum methane concentration is lower than atmospheric saturation (~1.6 mmol L^{-1} at 7 ºC; Yamamoto et al., 1976), which is consistent with the lack of gas bubbles observed in the vicinity of the Hugin Fracture, and there were no visual signs of degassing of sediments upon recovery. In cores with negligible sulfide, methane concentrations are <0.5 µmol L^{-1} (Figure 6d, Figure S1).

Concentrations of sulfate, which is the electron acceptor for anaerobic oxidation of methane, are lowest in cores that have highest sulfide concentrations (Figure 6a-e). In VC08, between 0.2 and 0.5 m sediment depth, sulfate is <1 mmol L^{-1} (Figure 6a) and methane was detected in this sediment interval. Sulfate concentrations increase again below the methane-rich zone reaching ~15 mmol L^{-1} below 2.5 m. This value is about 50% lower than in cores where no sulfide was found in the porewater. In core VC10, concentrations of sulfate are rather constant throughout the core (4-11 mmol L^{-1}, Figure 6b) and sulfide concentrations remain high. In VC14, where sulfide concentrations are only slightly above background, sulfate concentrations (10-15 mmol L^{-1}, Figure 6c) are ~50% lower than in cores without sulfide.

Most sediment porewaters have TA concentrations of 2.6 ±0.3 mmol L^{-1} and DIC concentrations of 2.6 ±0.1 mmol L^{-1}. However, much higher TA and DIC concentrations (19.5 and 13.0 mmol L^{-1}, respectively) are found in the upper 1.4 m of VC08, although they decrease to ~7.5 mmol L^{-1} (TA) and 6 mmol L^{-1} (DIC) below 2 m. In VC10 TA and DIC concentrations are also elevated, but are relatively constant (6-10 mmol L^{-1}) throughout the core. Both VC14 and VC28 have clearly elevated DIC and TA concentrations. Core VC23, from the abandoned

360 well 16/4-2, also has slightly elevated TA (3.5 mmol L^{-1}) and DIC (5 mmol L^{-1}), but no increase
361 of sulfide or decrease of sulfate is detected.

362 The $\delta^{13}C$ signatures of the porewater DIC range from -57‰ to 0‰ VPDB. Lowest
363 $\delta^{13}C_{DIC}$ values are found in porewaters with high sulfide and high methane (VC08, 0.8 m). Low
364 $\delta^{13}C_{DIC}$ values (~-50‰ VPDB) are also found in VC10. In the two other cores in which sulfide
365 was detected, $\delta^{13}C_{DIC}$ values are slightly less negative and range from -20 to -35‰ VPDB in
366 VC14 and from -12 to -40‰ VPDB in VC28. The $\delta^{13}C_{DIC}$ value of porewaters in sediments
367 close to the abandoned well 16/4-2 (VC23) is ~-5‰. In all other cores $\delta^{13}C_{DIC}$ signatures range
368 between -3 ±2‰ VPDB. In summary, all cores collected close to the Hugin Fracture (VC08,
369 VC10, VC14, VC28) show the presence of reduced fluids, i.e. high sulfide, TA and DIC
370 concentrations, low sulfate concentrations and a negative $\delta^{13}C_{DIC}$ signature. In contrast, cores
371 collected further away from the Hugin Fracture (e.g. VC04, Fig 6e) have seawater sulfate
372 concentrations and $\delta^{13}C_{DIC}$ signatures and low sulfide and methane concentrations. Site VC04 is
373 subsequently referred to as the 'background' site; other background sites are not discussed in
374 detail, but data from them are shown in Figure S1.
375
376 In cores that show the presence of reduced fluids, chloride concentrations are around 305
377 mmol L^{-1} ±16 mmol L^{-1} below 0.5 m (Figure 6a-e), which is lower than the chloride
378 concentration in the porewaters at the background sites (540 ±65 mmol L^{-1}). In the same cores,
379 concentrations of porewater Si and Ba are enriched up to 3-times (Si) and up to 40-times (Ba)
380 compared to background sites (Figure 6, Table 1). Dissolved ammonium is also 10-fold higher in
381 these cores (Figure 6). In contrast, other elements are depleted in the reduced fluids compared to
382 background concentrations, such as Li (0.6-times background), Sr (0.7-times background), Ca
383 (0.7-times background) and Mg (0.6-times background) (Figure 6). Concentrations of Fe only
384 slightly increased with depth at the background sites (Figure 6d), and were generally low in the
385 cores with reduced fluids (mostly <1 µmol L^{-1}, Figure 6a-d).
386
387 The Sr isotopic composition of porewaters from the background site VC04 is ~0.70915
388 to 0.70916, close to modern seawater (0.70918, Mokadem et al., 2015). Porewaters from sites
389 close to the Hugin Fracture tend to have slightly more radiogenic $^{87}Sr/^{86}Sr$ values, ranging from
390 0.70917 to 0.70928 (Figure 7, Table S2), with highest values measured in VC10. In VC08,
391 $^{87}Sr/^{86}Sr$ values are similar to VC10 in porewaters with highest sulfide concentrations, but they
392 are close to background site values below 2.6 m sediment depth.

393

394 **4.3.4 Composition of Utsira Formation waters**

395 Results of the analyses of the Utsira Formation waters are displayed in Table 1 together
396 with the compositions of background sediment porewaters and the reduced fluids sampled close
397 to the Hugin Fracture. Most notably, the Utsira Formation waters contain an order of magnitude
398 more Li and B relative to the background porewaters. Concentrations of Mg and Ca are slightly
399 lower than the background porewaters (0.4-0.8 times), and the formation waters have very low
400 sulfate concentrations (<0.5 mmol L^{-1}), but sulfide concentrations are below detection limit. In
401 contrast to many formation waters, Utsira Formation waters are not particularly saline, and their
402 Na-Cl content is close to that of seawater. The Sr isotopic composition ($^{87}Sr/^{86}Sr$) of Utsira
403 Formation water is 0.70924 (Figure 7), which is more radiogenic than modern-day seawater
404 (0.70918, Mokadem et al., 2015).

405

406 **5 Discussion**

407 **5.1 Hugin Fracture fluid composition and origin**

408 Our geochemical and geophysical analyses indicate that the Hugin Fracture is a site of
409 increased fluid flow activity and that reduced fluids are present in the near-surface sediments
410 along the fracture. The chemical composition of the porewaters can be used to assess the origin
411 of the fluids and to determine the extent to which their chemistry is modified by diagenetic and
412 biogeochemical processes occurring in the shallow subsurface.

413

414 **5.1.2 Fluid origin**

415 The connectivity of the Hugin Fracture with the strata below the Northland Shales, i.e.
416 below 550 m below the seafloor, can be assessed by comparison between the geochemical
417 composition of Utsira Formation fluids and porewaters in the shallow subsurface sediments
418 (Table 1). The Cl concentration of sediment porewaters in the vicinity of the Hugin Fracture is
419 ~50% lower than it is in the Utsira Formation fluids (~305 vs. ~540 mmol L^{-1}), and the
420 porewaters have far lower concentrations of Li and B. High levels of Li and B in the formation
421 fluids are likely due to reaction of the formation water with the reservoir sands: dissolution of B
422 and Li from silicate minerals occurs at moderate temperatures (50-350 °C; e.g. James et al.,
423 2003; Wimpenny et al., 2010). Rb is not usually leached at these temperature (James et al.,
424 2003), which is also consistent with our observations. The $^{87}Sr/^{86}Sr$ ratio of the formation water

425 is higher than that expected of Miocene-Pliocene-aged seawater (McArthur et al., 2001), which
426 is also consistent with input of radiogenic Sr from the reservoir sands. We conclude that Li and
427 B are likely to be effective tracers of Utsira Formation water, as they are enriched by an order of
428 magnitude compared to background porewaters, and are in general relatively unreactive during
429 transport through the overlying sediment column. However, as concentrations of both elements
430 are similar to seawater in the porewaters sampled along the Hugin Fracture (Table 1), we
431 conclude that Utsira Formation fluids are unlikely to be a source to the Hugin Fracture. Rather,
432 fluids circulating within shallow subsurface sediments along the fracture must originate from
433 within sediments located above the impermeable Northland Shale seal, i.e. < 550 m below the
434 seafloor.
435
436 A shallow fluid source is also suggested by the carbon isotopic composition of the DIC.
437 The carbon isotopic composition of methane ($\delta^{13}C_{CH4}$) in surface sediments sampled during
438 another expedition to the Hugin Fracture is between -85 and -32‰ VPDB, which indicates a
439 microbial source (Haeckel et al., 2013). The $\delta^{13}C_{CH4}$ value of methane discharged from
440 abandoned well 16/4-2 (-70‰ VPDB; Vielstädte et al., 2015) is within this range. Given that
441 methane from deep hydrocarbon reservoirs in the North Sea has a much higher (thermogenic)
442 $\delta^{13}C_{CH4}$ value (~-40‰ VPDB, James, 1990), and based on the thermal gradient in this area, the
443 microbial methane must be produced <2 km below the seafloor (Vielstädte et al., 2015).
444 Hydrogen carbonate ions produced by anaerobic oxidation of methane (Eq. 1) contribute to the
445 DIC content of sediment porewaters, and will have a carbon isotope signature that reflects that of
446 the methane from which it forms (Reeburgh, 2007). Our $\delta^{13}C_{DIC}$ analyses show that porewaters
447 from intervals with high sulfide concentrations have very low $\delta^{13}C_{DIC}$ values (~-57‰ VPDB)
448 compared to background values of 0‰ VPDB (Figure 6a). This strongly suggests that the
449 methane has a biogenic source. Shallow pockets of gas have been described in the Pliocene-
450 Pleistocene sediments above the Utsira Formation and may well be the source of the methane in
451 the shallow subsurface sediments (Karstens and Berndt, 2015, Vielstädte et al., 2015).
452
453 Further evidence that the source of the near-surface fluids in the Hugin Fracture lies
454 within younger sediments above the Northland Shale comes from their Cl concentrations;
455 porewaters from the Hugin Fracture have lower Cl concentrations compared to porewaters from
456 outside the fracture. Cl behaves conservatively in the marine environment, so the presence of
457 low Cl concentrations indicates that the porewaters in the Hugin Fracture have a different

458 source. Low-Cl fluids can be produced by dissolution of methane hydrates or ingression of
459 freshwater. Methane hydrate is unstable at the temperature and pressure conditions within the
460 shallow subsurface sediments in this area, but this area was likely covered by ice during some
461 parts of the last glacial period (e.g. Boulton & Hagedorn, 2006), so the sediments could contain a
462 freshwater component. The oxygen and deuterium isotopic compositions of porewaters from
463 within 10 cm of the seafloor also indicate the presence of meteoric water (Haeckel et al., 2013).
464

465 **5.2. Biogeochemical and diagenetic processes**

466 Black sediment patches and white microbial mats along the Hugin Fracture indicate the
467 presence of methane in the shallow subsurface sediments (Judd and Hovland, 2009) and
468 anaerobic oxidation of methane with sulfate close to the seafloor (Boetius et al., 2000).
469 Anaerobic oxidation of methane explains the low levels of methane and sulfate (VC08, Figure
470 6a) and the high concentrations of ^{13}C–depleted DIC and sulfide in all porewaters close to the
471 Hugin Fracture. In organic carbon-rich sediments, low concentrations of porewater sulfate and
472 high concentrations of porewater sulfide can be associated with sulfate reduction coupled to
473 anaerobic degradation of organic matter once other electron acceptors (oxygen, nitrate, Fe- and
474 Mn-oxides) have been depleted. However, this process does not seem to be important in this part
475 of the North Sea, as sulfide is not present in sediment porewaters outside the Hugin Fracture and
476 the carbon isotopic composition of the DIC (-57 ‰ VPDB) indicates a microbial methane source
477 (Reeburgh, 2007). Thus, although methane concentrations measured in our cores from the Hugin
478 Fracture are relatively low, DIC data provide evidence for its microbial conversion in the
479 shallow subsurface (Figure 6a).
480

481 Porewaters containing higher concentrations of sulfide (i.e. VC08, VC10; VC28; Figure
482 6) are also characterized by relatively low levels of Ca, which may indicate authigenic carbonate
483 precipitation due to the production of HCO_3^- during anaerobic methane oxidation (Eq. 1, Aloisi
484 et al., 2002; Luff and Wallmann, 2003). The increase of Ba in these fluids may be due to
485 dissolution of barite ($BaSO_4$), which is a potential substrate for methane oxidation below the
486 depth of sulfate depletion (Torres et al., 1996). However, there is no obvious loss of Ba from the
487 solid phase in the uppermost sediments (data not shown) and no authigenic carbonates were
488 found, so these reactions must have occurred elsewhere in the sedimentary overburden. These
489 Ca-depleted, Ba-enriched fluids indicate that part of the methane may have been removed deeper
490 in the sediments by anaerobic methane oxidation.

491

492 Oxidation of methane with sulfate usually results in a sharp transition from methane-rich
493 sulfate-free porewaters to overlying methane-poor sulfate-rich porewaters (the 'sulfate-methane
494 transition zone'; Borowski et al., 1996; Hensen et al., 2003). However, sulfate porewater
495 concentrations at some sites along the Hugin Fracture increase again below this transition zone
496 (Figure 6a), or sulfate has nearly constant concentrations in the upper part of the sediment
497 column (Figure 6c). In the same cores, methane concentrations remain at background values
498 (Figure 6a, c), except in VC08 where methane concentrations were <0.8 mmol L^{-1}. One
499 explanation for this pattern is that the methane-rich and the low-salinity fluids have a different
500 source. For example, in core VC14 (Figure 6c), concentrations of both sulfate and chloride are
501 ~50% lower than in the background sites, which implies that sulfate removal by methane deeper
502 in the sediment was not an important process. Sulfide re-oxidation could have occurred by an
503 unknown process in the deeper sediments, but $\delta^{13}C_{DIC}$ values (-20‰ VPDB) are significantly
504 higher than they are in the methane-rich intervals (-57‰ VPDB). At this site, concentrations of
505 total alkalinity and DIC are clearly higher than at the background sites and are consistent with
506 the effects of organic carbon diagenesis; this explanation is supported by higher than background
507 concentrations of ammonium, which is released during the remineralization of organic carbon
508 (e.g. Froehlich et al., 1979).

509

510 Hence we suggest that fluids circulating within the shallow subsurface sediments in the
511 vicinity of the Hugin Fracture come from two different sources: (i) A fluid that contains methane
512 that is mostly consumed by anaerobic methane oxidation, resulting in the higher concentrations
513 of porewater sulfide, TA and $\delta^{13}C$-depleted DIC. This fluid probably originates from shallow
514 gas pockets in the Pliocene-Pleistocene sediments. (ii) A fluid that has low levels of methane and
515 sulfide, low Cl, and slightly elevated levels of DIC and TA. This fluid may have entrained
516 glacial melt water that formed when the study area was located closer to the coastline or was
517 covered by ice. The presence of two different fluid sources is also supported by measurements of
518 porewater Sr isotope compositions. All porewaters from close to the Hugin Fracture are enriched
519 in radiogenic Sr compared to the background site, but fluids with low Cl tend to have higher
520 $^{87}Sr/^{86}Sr$ (~0.7928) than fluids that Cl concentrations close to seawater (~0.7920) (Figure 7,
521 Table S2). Fluids usually acquire radiogenic Sr isotope ratios during interactions with
522 continental crust or terrigenous material (Elderfield & Gieskes, 1982).

523

524 Geophysical imaging confirms that there are hotspots of gas or gas-enriched fluids, most
525 notably at the fault bend in the Hugin Fracture (Figures 3, 4). This fault bend thus potentially
526 represents a hydraulic connection to the shallow gas pockets in the Pliocene-Pleistocene
527 sediments above the Utsira Formation. We hypothesize that in the upper few meters of the
528 sediment a connected fracture network exists that transports reduced methane-enriched fluids.
529 Transport of these fluids likely occurs both horizontally as well as vertically, because the
530 dissolved sulfide distribution indicates that methane is only present in the upper 1 m of the
531 sediment in cores VC14 and VC28. Nevertheless there is evidence (i.e. higher sulfide, TA, DIC
532 concentrations and low $\delta^{13}C_{DIC}$ values) for anaerobic oxidation of methane at deeper depths in
533 core VC10. Horizontal transport of methane is facilitated by differences in the permeability
534 and/or porosity of different sediment layers; for example, methane-consumption is only observed
535 in distinct layers within subsurface sediments at the Tommeliten seep area (Niemann et al.,
536 2005). In the Hugin Fracture area, horizontal gas migration may occur in the shelly layer.
537
538 **5.2 Shallow fluid flow at the Hugin Fracture in a global context**
539 The presence of methane- and sulfide-containing, reduced fluids in shallow sediments
540 can have broad ecological and biological implications for the marine environment, providing
541 chemosynthetic energy to usually energy-depleted parts of the ocean, but potentially also
542 releasing a potent greenhouse gas into the water column and the atmosphere. In the Central and
543 Northern North Sea, the presence of methane and its oxidation products in shallow subsurface
544 sediments and methane release to the water column has been demonstrated at seabed pockmarks
545 (Hovland et al., 2012) and at abandoned hydrocarbon exploration wells (e.g. Vielstädte et al.,
546 2015). The discovery of reduced fluids and evidence for the presence of shallow methane (high
547 sulfide concentrations, bacterial mats) in the Hugin Fracture sediments suggests that fractures
548 may also be important fluid migration pathways in the North Sea. Fault-related methane seepage
549 structures have mainly been observed in tectonically active areas such as the Marmara Sea
550 (Dupre et al., 2015), the Santa Barbara Basin (Eichhubl et al., 2000) and the Nankai Trough
551 (Henry et al., 2002). Our study shows that the Hugin Fracture is an active conduit transferring
552 fluids from the deeper in the sediment column (<500 m below the seafloor) into surface
553 sediments, with visual and geophysical indicators for near-surface fluid flow, biogeochemical
554 turnover of methane and large spatial variabilities.
555

Above sites of focused methane discharge, such as the Håkon Mosby mud volcano (Sauter et al., 2006) and mud volcanoes in the Gulf of Cadiz (Sommer et al., 2009), methane concentrations can be >10,000 nmol L^{-1}. In the North Sea, background dissolved methane concentrations are typically ~ 5-10 nmol L^{-1} (von Deimling et al., 2011); concentrations as high as 400,000 nmol L^{-1} have been measured at North Sea blow-out sites (von Deimling et al., 2015). In the vicinity of the Hugin Fracture methane concentrations reach up to 3160 nmol L^{-1} (Figure 5), which indicates that part of the methane in the shallow sub-seabed sediments in the vicinity of the fracture is not consumed by the microbial filter in the sediments, but is transferred to the water column. The lack of gas flares in the water column close to the fracture suggests that the majority of the methane emitted from the sediments is probably in dissolved form as found at other seep locations (McGinnis et al., 2006, Sauer et al., 2015) or that methane emissions are ephemeral. Ephemeral gas emissions have been observed at the Marmara fault (Dupre et al., 2015).

From the lack of gas bubbles, the relatively low methane concentrations measured in the water column, and the evidence for anaerobic oxidation of methane in sediment porewaters, we conclude that the methane supply to the fracture is medium to low. If the methane flux is relatively low, then the sulfate flux from seawater into the sediment is high enough to consume most of the methane. At the Hugin Fracture the sediment porewaters are not completely sulfate depleted, and sulfide concentrations (0.3 - 6 mmol L^{-1}) are relatively low compared to other cold seeps (e.g. >12 mmol L^{-1} at Håkon Mosby Mud Volcano and the Amon Mud Volcano (Felden et al., 2013; Lichtschlag et al., 2010), ~20 mmol L^{-1} in the Gulf of Mexico (Aharon and Fu, 2000), ~6 mmol L^{-1} at the Tommeliten Field (Niemann et al.. 2005)).

The distribution of microbial mats along the Hugin Fracture is patchy, suggesting that the methane flux may also be spatially variable. Highest porewater sulfide concentrations are found at different depths at different sites (0.3-1 mbsf), and are variable (0.3 - 6 mmol L^{-1}). Trapping of methane below microbial mats can also result in heterogeneities in the methane distribution in sediments, as reported for other parts of the North Sea (Hovland, 2002). Nevertheless, if mats are visible, sulfide must be present close to the sediment surface so that the oxygen- and nitrate-dependent, sulfide oxidizing bacteria can thrive. The absence of microbial mats does not necessarily indicate the absence of sulfide production; if reactive iron-minerals are present in the sediments, dissolved sulfide can be immobilized in the form of iron-sulfide minerals and may

589 not reach the sediment surface (Fe-S solid phase peaks Figure 6a, b, d). Over time, this barrier
590 may be overcome as the supply of reactive iron-minerals is depleted, allowing bacterial mats to
591 form on top of the sediments. Taking into account the total length of the Hugin Fracture (3 km),
592 and assuming that reduced fluids are found within 5-10 m either side of the fracture as suggested
593 by the AUV imagery, the area of the Hugin Fracture that contains reduced, sulfide-rich fluids
594 comprises up to 0.03-0.06 km^2 of the seafloor. This areal extent is likely to be a minimum
595 estimate because, as discussed above, precipitation of sulfides may prevent the formation of
596 bacterial mats at the seafloor. This area is slightly smaller than other known methane seeps area
597 in the North Sea, such as the 'Heincke' site (0.1 km^2) and Tommeliten (0.12 km^3); however,
598 active seepage only occurs over a fraction of their surface area (Hovland et al., 2012, Judd and
599 Hovland, 2009) so the Hugin Fracture may be of similar importance as a chemosynthetic hotspot
600 as other fluid flow structures in the North Sea.
601
602 **5.3 Monitoring of fluid flow across the seabed**
603 There is an increasing need to develop accurate and cost-effective monitoring
604 technologies that can be reliably used to quantify the extent and flux of reduced, methane-rich
605 fluids to shallow sediments. Although the Central North Sea is extremely well-surveyed, the
606 Hugin Fracture was discovered only recently (Pedersen et al., 2013). Here, we show that the
607 fracture hosts reduced fluids in the near-surface sediments and the areal extent of these fluids
608 may be similar to that of much larger features such as pockmarks. By comparing the different
609 geochemical and geophysical approaches that were applied in the survey of the Hugin Fracture,
610 we have identified various effective monitoring strategies:

611 • AUVs may be used to locate and investigate fluid flow structures using geophysical and
612 geochemical sensing instruments.
613
614 • Formation waters often have a different geochemical composition from the surface
615 porewaters, and relatively unreactive chemical species such as Li or B can be used to trace the
616 origin, depth and connectivity of deep reservoirs with the sediment overburden. Knowledge
617 of the composition of formation fluids may be important for assessing the integrity of
618 subseafloor CO_2 storage sites.
619

620 • The chemical composition of sediment porewaters allows different fluid sources to be
621 distinguished.
622
623 • The absence of gas bubbles, microbial mats and sediment black spots does not necessarily
624 indicate the absence of fluid transport into shallow subsurface sediments, as fluid flow can be
625 variable in space and time. Porewater chemistry can reveal the presence of reduced fluids in
626 the subsurface, even if there is no surface expression.
627
628 • Along the Hugin Fracture, methane anomalies in the water column have been detected using
629 traditional sampling techniques from a ship, but these may not be suitable for detecting
630 smaller point sources (such as the abandoned wells). Source localization at smaller scales
631 requires more advanced methods, such as sensors mounted on AUVs.

Acknowledgements

We thank the crew and master of RRS James Cook for their invaluable work during the JC77 cruise. We would also like to acknowledge the help of the AUV team, the BGS vibrocorer team and the scientific party during this cruise. We thank Belinda Alker, Tim Le Bas, Ambra Milani, Mario Esposito, Mark Hopwood, Matt Cooper, Suzie MacLachlan and Mark Vardy for their assistance on board and technical support in the laboratory. The British Ocean Sediment Core Research Facility (BOSCORF) is thanked for using their facilities. Special thanks are due to the Volve production support team and Aina Dahlø Janbu for help with the formation water sampling. Data supporting the conclusions drawn in this manuscript can be found in the Tables, the supporting materials are deposited in the Earth System database www.PANGAEA.de (https://doi.org/10.1594/PANGAEA.883560). This work was financially supported by the European Community's the ECO2 project (grant agreement no. 265847).

Conflict of interest statement

The authors declare that the research was conducted in the absence of any commercial or financial relationships that could be construed as a potential conflict of interest.

650 **References**

651 Aharon, P. and Fu, B.: Microbial sulfate reduction rates and sulfur and oxygen isotope
652 fractionations at oil and gas seeps in deepwater Gulf of Mexico, Geochimica et
653 Cosmochimica Acta, 64, 233-246, 2000.

654 Aloisi, G., Bouloubassi, I., Heijs, S. K., Pancost, R. D., Pierre, C., Damsté, J. S. S., Gottschal, J.
655 C., Forney, L. J., and Rouchy, J.-M.: CH_4-consuming microorganisms and the formation of
656 carbonate crusts at cold seeps, Earth and Planetary Science Letters, 203, 195-203, 2002.

657 Boetius, A., Ravenschlag, K., Schubert, C. J., Rickert, D., Widdel, F., Gieseke, A., Amann, R.,
658 Jørgensen, B. B., Witte, U., and Pfannkuche, O.: A marine microbial consortium apparently
659 mediating anaerobic oxidation of methane, Nature, 407, 623-626, 2000.

660 Borowski, W. S., Paull, C. K., and Ussler, W.: Marine pore-water sulfate profiles indicate in situ
661 methane flux from underlying gas hydrate, Geology, 24, 655-658, 1996.

662 Boulton, G., & Hagdorn, M.: Glaciology of the British Isles Ice Sheet during the last glacial
663 cycle: form, flow, streams and lobes. Quaternary Science Reviews, 25, 3359-3390, 2006.

664 Cartwright, J.: Diagenetically induced shear failure of fine-grained sediments and the
665 development of polygonal fault systems, Marine and Petroleum Geology, 28, 1593-1610,
666 2011.

667 Cartwright, J. A.: Episodic basin-wide fluid expulsion from geopressured shale sequences in the
668 North Sea basin, Geology, 22, 447-450, 1994.

669 Cavanagh, A. J. and Haszeldine, R. S.: The Sleipner storage site: Capillary flow modeling of a
670 layered CO_2 plume requires fractured shale barriers within the Utsira Formation, International
671 Journal of Greenhouse Gas Control, 21, 101-112, 2014.

672 Cevatoglu, M., Bull, J. M., Vardy, M. E., Gernon, T. M., Wright, I. C., and Long, D.: Gas
673 migration pathways, controlling mechanisms and changes in sediment acoustic properties
674 observed in a controlled sub-seabed CO_2 release experiment, International Journal of
675 Greenhouse Gas Control, 38, 26-43, 2015.

676 Chadwick, R., Zweigel, P., Gregersen, U., Kirby, G., Holloway, S., and Johannessen, P.:
677 Geological reservoir characterization of a CO_2 storage site: the Utsira Sand, Sleipner,
678 northern North Sea, Energy, 29, 1371-1381, 2004.

679 Chen, J., Song, H., Guan, Y., Yang, S., Pinheiro, L. M., Bai, Y., Liu, B., and Geng, M.:
680 Morphologies, classification and genesis of pockmarks, mud volcanoes and associated fluid
681 escape features in the northern Zhongjiannan Basin, South China Sea, Deep Sea Research
682 Part II: Topical Studies in Oceanography, 122, 106-117, 2015.

683 Ciais P., Sabine C., Bala G., Bopp L., Brovkin V., Canadell J., Chhabra A., DeFries R.,
684 Galloway J., Heimann M., Jones C.: Carbon and other biogeochemical cycles. In Climate
685 change 2013: the physical science basis. Contribution of Working Group I to the Fifth
686 Assessment Report of the Intergovernmental Panel on Climate Change 2014 Apr (pp. 465-
687 570). Cambridge University Press, 2014.

688 Cline, J. D.: Spectrophotometric determination of hydrogen sulfide in natural waters, Limnol
689 Oceanogr, 14, 454-&, 1969.

690 Croudace, I. W., Rindby, A., and Rothwell, R. G.: ITRAX: description and evaluation of a new
691 multi-function X-ray core scanner, Special publication-geological society of London, 267, 51,
692 2006.

693 Dowdeswell, J. and Ottesen, D.: Buried iceberg ploughmarks in the early Quaternary sediments
694 of the central North Sea: a two-million year record of glacial influence from 3D seismic data,
695 Marine Geology, 344, 1-9, 2013.

696 Dupré, S., Mascle, J., Foucher, J.-P., Harmegnies, F., Woodside, J., and Pierre, C.: Warm brine
697 lakes in craters of active mud volcanoes, Menes caldera off NW Egypt: evidence for deep-
698 rooted thermogenic processes, Geo-Marine Letters, 34, 153-168, 2014.

699 Eichhubl, P., Greene, H., Naehr, T., and Maher, N.: Structural control of fluid flow: offshore
700 fluid seepage in the Santa Barbara Basin, California, Journal of Geochemical Exploration, 69,
701 545-549, 2000.

702 Elderfield, H. and Gieskes, J. M.: Sr isotopes in interstitial waters of marine sediments from
703 Deep Sea Drilling Project cores, Nature, 300, 493-497, 1982.

704 Etiope, G., Lassey, K. R., Klusman, R. W., and Boschi, E.: Reappraisal of the fossil methane
705 budget and related emission from geologic sources, Geophysical Research Letters, 35, 2008.

706 Felden, J., Lichtschlag, A., Wenzhöfer, F., de Beer, D., Feseker, T., Pop Ristova, P., De Lange,
707 G., and Boetius, A.: Limitations of microbial hydrocarbon degradation at the Amon mud
708 volcano (Nile deep-sea fan), Biogeosciences, 10, 3269-3283, 2013.

709 Froelich, P., Klinkhammer, G. P., Bender, M. L., Luedtke, N. A., Heath, G. R., Cullen, D., ... &
710 Maynard, V. Early oxidation of organic matter in pelagic sediments of the eastern equatorial
711 Atlantic: suboxic diagenesis. Geochimica et Cosmochimica Acta, 43, 1075-1090, 1979.

712 Gutowski, M., Bull, J., Henstock, T., Dix, J., Hogarth, P., Leighton, T., and White, P.: Chirp
713 sub-bottom profiler source signature design and field testing, Marine Geophysical
714 Researches, 23, 481-492, 2002.

715 Grünke, S., Felden, J., Lichtschlag, A., Girnth, A. C., De Beer, D., Wenzhöfer, F., and Boetius,
716 A.: Niche differentiation among mat-forming, sulfide-oxidizing bacteria at cold seeps of the
717 Nile Deep Sea Fan (Eastern Mediterranean Sea), Geobiology, 9, 330-348, 2011.

718 Haeckel, M., Wallmann, K., Schmidt, M., Liebetrau, V., Sommer, S., Schroller, D., Schoenfeld,
719 J., Karstens, J., and Berndt, C.: Fluid expulsion at a 3-km long fracture system in the Northern
720 North Sea - geochemical constraints on the origin of gas and water, AGU Fall Meeting, San
721 Fransisco, USA, 2013.

722 Harrington, J.F., Noy, D.J., Horseman, S.T., Birchall, D.J., Chadwick, R.A.: Laboratory study of
723 gas and water flow in the Nordland Shale, Sleipner, North Sea. In: Carbon Dioxide
724 Sequestration in Geological Media–State of the Science. In: AAPG Studies in Geology,
725 vol.59, 2009

726 Henry, P., Lallemant, S., Nakamura, K.-i., Tsunogai, U., Mazzotti, S., and Kobayashi, K.:
727 Surface expression of fluid venting at the toe of the Nankai wedge and implications for flow
728 paths, Marine Geology, 187, 119-143, 2002.

729 Heggland, R.: Detection of gas migration from a deep source by the use of exploration 3D
730 seismic data, Marine Geology, 137, 41-47, 1997.

731 Hensen, C., Zabel, M., Pfeifer, K., Schwenk, T., Kasten, S., Riedinger, N., Schulz, H. D., and
732 Boetius, A.: Control of sulfate pore-water profiles by sedimentary events and the significance

733 of anaerobic oxidation of methane for the burial of sulfur in marine sediments, Geochimica et
734 Cosmochimica Acta, 67, 2631-2647, 2003.

735 Hovland, M., & Sommerville, J. H.: Characteristics of two natural gas seepages in the North Sea.
736 Marine and Petroleum Geology, 2(4), 319-326, 1985.

737 Hovland, M.: On the self-sealing nature of marine seeps, Continental Shelf Research, 22, 2387-
738 2394, 2002.

739 Hovland, M., & Svensen, H.: Submarine pingoes: Indicators of shallow gas hydrates in a
740 pockmark at Nyegga, Norwegian Sea. Marine Geology, 228, 15-23, 2006.

741 Hovland, M., Jensen, S., and Fichler, C.: Methane and minor oil macro-seep systems — Their
742 complexity and environmental significance, Marine Geology, 332–334, 163-173, 2012.

743 James, A. T.: Correlation of reservoired gases using the carbon isotopic compositions of wet gas
744 components (1), AAPG bulletin, 74, 1441-1458, 1990.

745 James, R. H., Allen, D. E., and Seyfried, W.: An experimental study of alteration of oceanic
746 crust and terrigenous sediments at moderate temperatures (51 to 350 °C): Insights as to
747 chemical processes in near-shore ridge-flank hydrothermal systems, Geochimica et
748 Cosmochimica Acta, 67, 681-691, 2003.

749 Judd, A. and Hovland, M.: Seabed Fluid Flow. The impact on geology, biology and the marine
750 environment, Cambridge University Press. , 2009.

751 Justwan, H. and Dahl, B.: Quantitative hydrocarbon potential mapping and organofacies study in
752 the Greater Balder Area, Norwegian North Sea, 2005, 1317-1329.

753 Karstens, J. and Berndt, C.: Seismic chimneys in the Southern Viking Graben–Implications for
754 palaeo fluid migration and overpressure evolution, Earth and Planetary Science Letters, 412,
755 88-100, 2015.

756 Krämer, K., Holler, P., Herbst, G., Bratek, A., Ahmerkamp, S., Neumann, A., Bartholomä, A.,
757 van Beusekom, J.E.E., Holtappels, M. and Winter, C.: Abrupt emergence of a large pockmark
758 field in the German Bight, southeastern North Sea. Scientific Reports 7, 5150, 2017

759 Kvenvolden, K. A. and Rogers, B. W.: Gaia's breath—global methane exhalations, Marine and
760 Petroleum Geology, 22, 579-590, 2005.

761 Landschulze, K. and Pedersen, R.: Caprock integrity for offshore CO_2 storage in the Norwegian
762 North Sea-Seismic investigation of a soft sediment seafloor fracture, AGU Fall Meeting, San
763 Fransisco, USA, 2013.

764 Landschulze, K., Tveranger, J., and Pedersen, R.: Characterization of Shallow Seal Complexes
765 for CO_2 Storage Sites–Example from the Greater Sleipner Area, 2014.

766 Lichtschlag, A., Felden, J., Brüchert, V., Boetius, A., and De Beer, D.: Geochemical processes
767 and chemosynthetic primary production in different thiotrophic mats of the Håkon Mosby
768 Mud Volcano (Barents Sea), Limnol Oceanogr, 2010.

769 Lonergan, L., Maidment, S. C., and Collier, J. S.: Pleistocene subglacial tunnel valleys in the
770 central North Sea basin: 3-D morphology and evolution, Journal of Quaternary Science, 21,
771 891-903, 2006.

772 Luff, R. and Wallmann, K.: Fluid flow, methane fluxes, carbonate precipitation and
773 biogeochemical turnover in gas hydrate-bearing sediments at Hydrate Ridge, Cascadia

774 Margin: numerical modeling and mass balances, Geochimica et Cosmochimica Acta, 67,
775 3403-3421, 2003.

776 Mattey, D., Lowry, D., Duffet, J., Fisher, R., Hodge, E., and Frisia, S.: A 53 year seasonally
777 resolved oxygen and carbon isotope record from a modern Gibraltar speleothem:
778 Reconstructed drip water and relationship to local precipitation, Earth and Planetary Science
779 Letters, 269, 80-95, 2008.

780 McArthur, J., Howarth, R., and Bailey, T.: Strontium isotope stratigraphy: LOWESS version 3:
781 best fit to the marine Sr-isotope curve for 0–509 Ma and accompanying look-up table for
782 deriving numerical age, The Journal of Geology, 109, 155-170, 2001.

783 McGinnis, D. F., Greinert, J., Artemov, Y., Beaubien, S., and Wüest, A.: Fate of rising methane
784 bubbles in stratified waters: How much methane reaches the atmosphere?, Journal of
785 Geophysical Research: Oceans, 111, 2006.

786 Mokadem, F., Parkinson, I. J., Hathorne, E. C., Anand, P., Allen, J. T., and Burton, K. W.: High-
787 precision radiogenic strontium isotope measurements of the modern and glacial ocean: Limits
788 on glacial–interglacial variations in continental weathering, Earth and Planetary Science
789 Letters, 415, 111-120, 2015.

790 Nicoll, G. D.: Evaluation of the Nordland Group overburden as an effective seal for the Sleipner
791 CO_2 storage site (offshore Norway) using analytical and stochastic modelling techniques,
792 2012. University of Edinburgh, 2012

793 Niemann, H., Elvert, M., Hovland, M., Orcutt, B., Judd, A., Suck, I., Gutt, J., Joye, S., Damm,
794 E., and Finster, K.: Methane emission and consumption at a North Sea gas seep (Tommeliten
795 area), Biogeosciences Discussions, 2, 1197-1241, 2005.

796 Pedersen, R., Blomberg, A., Landschulze, K., Baumberger, T., Oekland, I., Reigstad, L.,
797 Gracias, N., Moerkved, P., Stensland, A., and Lilley, M.: Discovery of 3 km long seafloor
798 fracture system in the Central North Sea, AGU Fall Meeting, San Fransisco, USA, 2013.

799 Pierre, C., Bayon, G., Blanc-Valleron, M.-M., Mascle, J., and Dupré, S.: Authigenic carbonates
800 related to active seepage of methane-rich hot brines at the Cheops mud volcano, Menes
801 caldera (Nile deep-sea fan, eastern Mediterranean Sea), Geo-Marine Letters, 34, 253-267,
802 2014.

803 Praeg, D.: Seismic imaging of mid-Pleistocene tunnel-valleys in the North Sea Basin—high
804 resolution from low frequencies, Journal of Applied Geophysics, 53, 273-298, 2003.

805 Quinn, R., Bull, J., and Dix, J.: Optimal processing of marine high-resolution seismic reflection
806 (Chirp) data, Marine Geophysical Researches, 20, 13-20, 1998.

807 Reeburgh, W. S.: Oceanic methane biogeochemistry. Chemical reviews, 107(2), 486-513, 2007.

808 Sauer, S., Knies, J., Lepland, A., Chand, S., Eichinger, F., & Schubert, C. J.: Hydrocarbon
809 sources of cold seeps off the Vesterålen coast, northern Norway. Chemical Geology, 417,
810 371-382, 2015.

811 Schroot, B. M., Klaver, G. T., and Schüttenhelm, R. T.: Surface and subsurface expressions of
812 gas seepage to the seabed—examples from the Southern North Sea, Marine and Petroleum
813 Geology, 22, 499-515, 2005.

Schwietzke, S., Sherwood, O. A., Bruhwiler, L. M., Miller, J. B., Etiope, G., Dlugokencky, E. J., Michel, S. E., Arling, V. A., Vaughn, B. H., and White, J. W.: Upward revision of global fossil fuel methane emissions based on isotope database, Nature, 538, 88-91, 2016.

Sauter, E. J., Muyakshin, S. I., Charlou, J.-L., Schlüter, M., Boetius, A., Jerosch, K., Damm, E., Foucher, J.-P., and Klages, M.: Methane discharge from a deep-sea submarine mud volcano into the upper water column by gas hydrate-coated methane bubbles, Earth and Planetary Science Letters, 243, 354-365, 2006.

Sejrup, H., Larsen, E., Landvik, J., King, E., Haflidason, H., and Nesje, A.: Quaternary glaciations in southern Fennoscandia: evidence from southwestern Norway and the northern North Sea region, Quaternary Science Reviews, 19, 667-685, 2000.

Sommer, S., Linke, P., Pfannkuche, O., Schleicher, T., Schneider, J., Reitz, A., Haeckel, M., Flögel, S., and Hensen, C.: Seabed methane emissions and the habitat of frenulate tubeworms on the Captain Arutyunov mud volcano (Gulf of Cadiz), Marine Ecology Progress Series, 382, 69-86, 2009.

Sommer, S., Schmidt, M., and Linke, P.: Continuous inline mapping of a dissolved methane plume at a blowout site in the Central North Sea UK using a membrane inlet mass spectrometer–Water column stratification impedes immediate methane release into the atmosphere, Marine and Petroleum Geology, 68, 766-775, 2015.

Skarke, A., Ruppel, C., Kodis, M., Brothers, D., and Lobecker, E.: Widespread methane leakage from the sea floor on the northern US Atlantic margin, Nature Geoscience, 7, 657-661, 2014.

Swinnerton, J. W., and Linnenbom, V. J.: Determination of the C1 to C4 hydrocarbons in sea water by gas chromatography. Journal of Gas Chromatography 5, 570-573, 1967.

Torres, M. E., Bohrmann, G., and Suess, E.: Authigenic barites and fluxes of barium associated with fluid seeps in the Peru subduction zone, Earth and Planetary Science Letters, 144, 469-481, 1996.

Tóth, Z., Spieß, V., and Jensen, J.: Seismo-acoustic signatures of shallow free gas in the Bornholm Basin, Baltic Sea, Continental Shelf Research, 88, 228-239, 2014.

Vanneste, M., Sultan, N., Garziglia, S., Forsberg, C. F., and L'Heureux, J.-S.: Seafloor instabilities and sediment deformation processes: the need for integrated, multi-disciplinary investigations, Marine Geology, 352, 183-214, 2014.

Vielstädte, L., Karstens, J., Haeckel, M., Schmidt, M., Linke, P., Reimann, S., Liebetrau, V., McGinnis, D. F., and Wallmann, K.: Quantification of methane emissions at abandoned gas wells in the Central North Sea, Marine and Petroleum Geology, 2015.

von Deimling, J. S., Linke, P., Schmidt, M., and Rehder, G.: Ongoing methane discharge at well site 22/4b (North Sea) and discovery of a spiral vortex bubble plume motion, Marine and Petroleum Geology, 68, 718-730, 2015.

von Deimling, J. S., Rehder, G., Greinert, J., McGinnnis, D., Boetius, A., and Linke, P.: Quantification of seep-related methane gas emissions at Tommeliten, North Sea, Continental Shelf Research, 31, 867-878, 2011.

Wiggins, S. M., Leifer, I., Linke, P., and Hildebrand, J. A.: Long-term acoustic monitoring at North Sea well site 22/4b, Marine and Petroleum Geology, 68, 776-788, 2015.

Wimpenny, J., Gíslason, S. R., James, R. H., Gannoun, A., Von Strandmann, P. A. P., and Burton, K. W.: The behaviour of Li and Mg isotopes during primary phase dissolution and

857 secondary mineral formation in basalt, Geochimica et Cosmochimica Acta, 74, 5259-5279,
858 2010.

859 Wiprut, D. and Zoback, M. D.: Fault reactivation and fluid flow along a previously dormant
860 normal fault in the northern North Sea, Geology, 28, 595-598, 2000.

861 Yamamoto, S., Alcauskas, J. B., and Crozier, T. E.: Solubility of methane in distilled water and
862 seawater, Journal of Chemical & Engineering Data, 21, 78-80, 1976.
863

864

865 **Tables**

866 **Table 1:** Geochemical composition of Utsira Formation waters (well 15/9-F-07 and 15/9-F-09)
867 compared to the composition of porewaters in the upper 3 m of the background sites (average of
868 VC01, VC04, VC12, VC15, VC16, VC20, VC24) and advected fluids (VC04, VC08, VC14,
869 VC28). n.d.=not determined, b.d.=below detection. *$^{87}Sr/^{86}Sr$ data for formation fluids are from
870 an earlier sampling campaign in 2011.

871

Species	Utsira Formation water 15/9-F-07	Utsira Formation water 15/9-F-09	Background sediment porewater	Hugin Fracture porewater
Cations				
Li (µmol kg^{-1})	424	341	27 ±3	31
B (µmol kg^{-1})	1557	1449	400 ±51	475
Na (mmol kg^{-1})	491	485	474 ±50	338
Mg (mmol kg^{-1})	24	22	53 ±6	33.5
Ca (mmol kg^{-1})	11.4	10.1	12.3 ±1.3	5.5
Rb (µmol kg^{-1})	0.9	0.8	n.d.	n.d.
Sr (µmol kg^{-1})	104	99	88 ±9	61
Ba (µmol kg^{-1})	4.5	2.1	0.2 ±0.2	7.6
Anions				
Cl (mmol L^{-1})	533	518	540 ±65	247
Br (µmol L^{-1})	1273	1208	870 ±108	400
SO_4 (mmol L^{-1})	0.05	0.01	27.48 ±3.36	0.28
Carbonate System				
pH	7	7	n.d.	n.d.
DIC (mmol L^{-1})	16.6	18.2	2.6 ±0.1	13.0
TA (mmol L^{-1})	16.2	19.3	2.6 ±0.3	19.5
Nutrients				
Phosphate (µmol L^{-1})	0.7	0.8	6 ±4	35
Silicate (µmol L^{-1})	274	317	100 ±38	310
NO_x (µmol L^{-1})	b.d.	b.d	8 ±6	28
Other parameters				
Sulfide (µmol L^{-1})	b.d	b.d	b.d	5971
T (°C)	29.5	29.3	n.d.	n.d.
$^{87}Sr/^{86}Sr$*	0.70924	0.70924	0.70916	0.70928

872 **Figure Captions**

873 **Figure 1:** (a) Map of the area, (b) with side-scan imagery of the Hugin Fracture Area and the
874 abandoned well 16/4-2, (c) the Hugin Fracture detailed area and (d) an interpretation of the
875 detailed area. The two main fault segments and the fault bend location are indicated. The Hugin
876 Fracture is indicated by the solid red line; the possible surficial fault extent is indicated by the
877 red dotted line. The abandoned well 16/4-2 is indicated by the red star.

878 **Figure 2:** Autosub 6000 pictures acquired within the Hugin Fracture area (Dive M62, flying
879 altitude 3 m). The seabed sediments mainly comprise sandy sediments (a), and shell hashes
880 (white backscatter) (b), however locally along the Hugin Fracture, and well 16/4-2 where there is
881 increased fluid flow activity bacterial mats and reduced sediments (dark spotting) are seen (c-j).
882 The abandoned well 16/4-2 is indicated by the red star.

883 **Figure 3:** Autosub AUV Chirp reflection profiles exhibiting acoustic amplitude anomalies
884 within the top 5 m of the sub-surface. (a) Profile across the Hugin Fracture, with enhanced
885 reflectivity in the down-thrown side; (b) zoomed wiggle trace view showing enhanced
886 reflectivity.

887 **Figure 4:** RMS seismic amplitude anomalies from Chirp seismic reflection data within the
888 Hugin Fracture area. The RMS amplitude is calculated from the seabed return down to 3 ms
889 Two Way Time below the seabed. Seismic amplitude anomalies are detected along the Hugin
890 Fracture (solid line) and at the abandoned well site (star). Locations of the possible surficial fault
891 extent of the Hugin Fracture (black dotted line), and VC locations (dots) are shown.

892 **Figure 5:** Methane concentrations in the water column: (a) Transect from the southern part of
893 the area south of the Hugin Fracture up to the Hugin Fracture in the North; (b) W-E transect
894 following the Hugin Fracture surface expression.

895 **Figure 6:** Composition of sediments and sediment porewaters in areas with active fluid flow
896 along the Hugin Fracture; (a) VC08, (b) VC10, (c) VC14, (d) VC28) and a background site close
897 to the Hugin Fracture; (e) VC04. The dashed vertical lines show the concentration measured in
898 the background site. Note different scales for sulfide. Sediment and porewater geochemistry of
899 other cores taken outside the Hugin Fracture, close to the abandoned well and in the area south
900 of the Hugin Fracture are displayed in Figure S2. All data are deposited in the Earth System
901 database www.PANGAEA.de (https://doi.org/10.1594/PANGAEA.883560).

902 **Figure 7:** Sr isotope ($^{87}Sr/^{86}Sr$) variation with depth in sediment porewaters. VC10, VC08 and
903 VC14 are characterized by fluid flow; in VC08 methane is present in the upper 1 m and in VC10
904 methane is absent; in both cores sulfide concentrations are relatively high. In VC14 methane and
905 sulfide concentrations are low. VC04 is the background site. Seawater $^{87}Sr/^{86}Sr$ is shown by the
906 dashed line (Mokadem et al., 2015) and the $^{87}Sr/^{86}Sr$ composition of Utsira Formation waters is
907 shown by the dotted line.

Figure1.

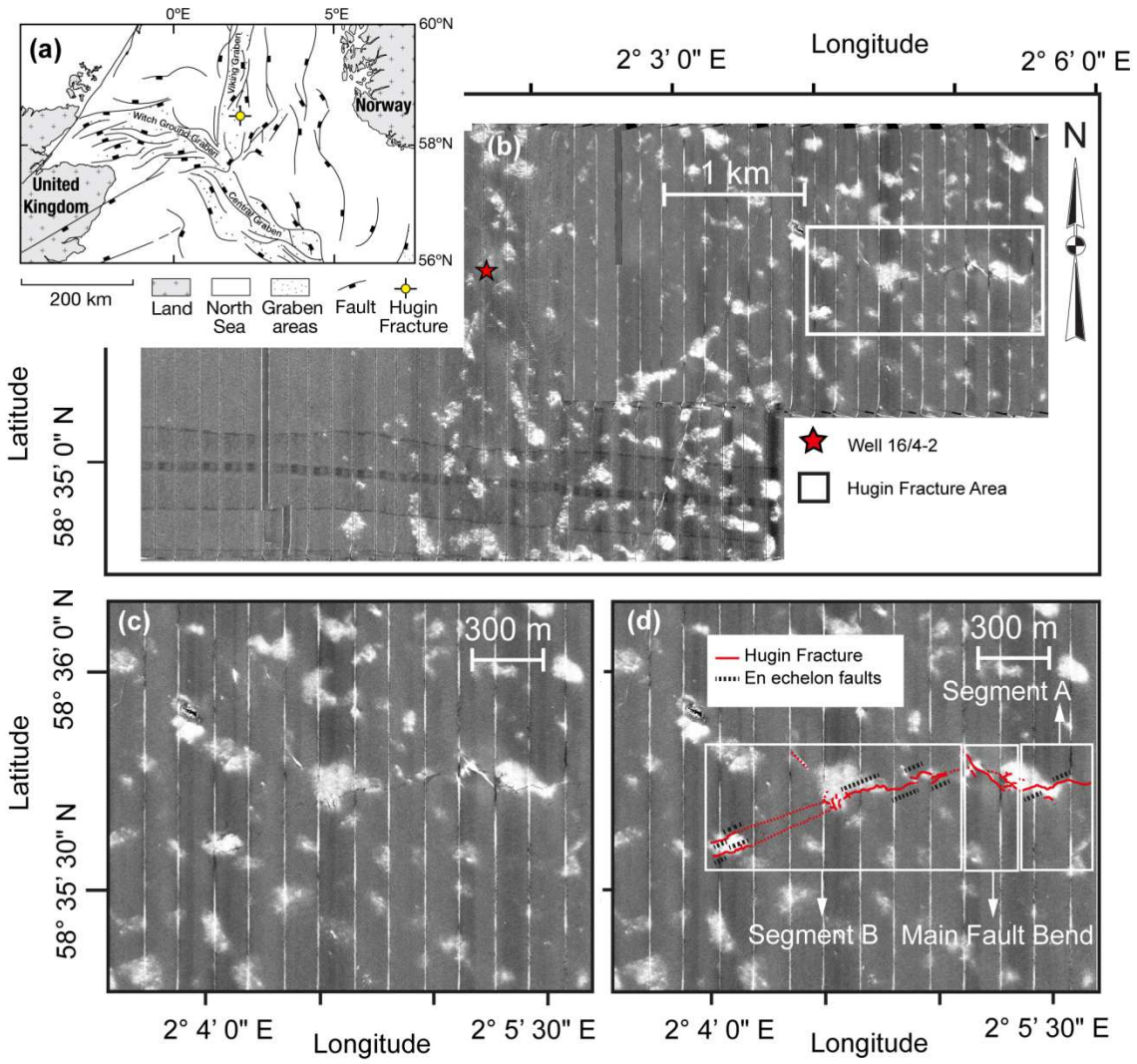
(a)
0°E
5°E
60°N
58°N
56°N
Viking Graben
Witch Ground Graben
Central Graben
Norway
United Kingdom
200 km
Land
North Sea
Graben areas
Fault
Hugin Fracture
(b)
1 km
N
Well 16/4-2
Hugin Fracture Area
Latitude
58° 35' 0" N
2° 3' 0" E
Longitude
2° 6' 0" E
(c)
300 m
58° 36' 0" N
58° 35' 30" N
2° 4' 0" E
2° 5' 30" E
(d)
300 m
Hugin Fracture
En echelon faults
Segment A
Segment B
Main Fault Bend

Figure2.

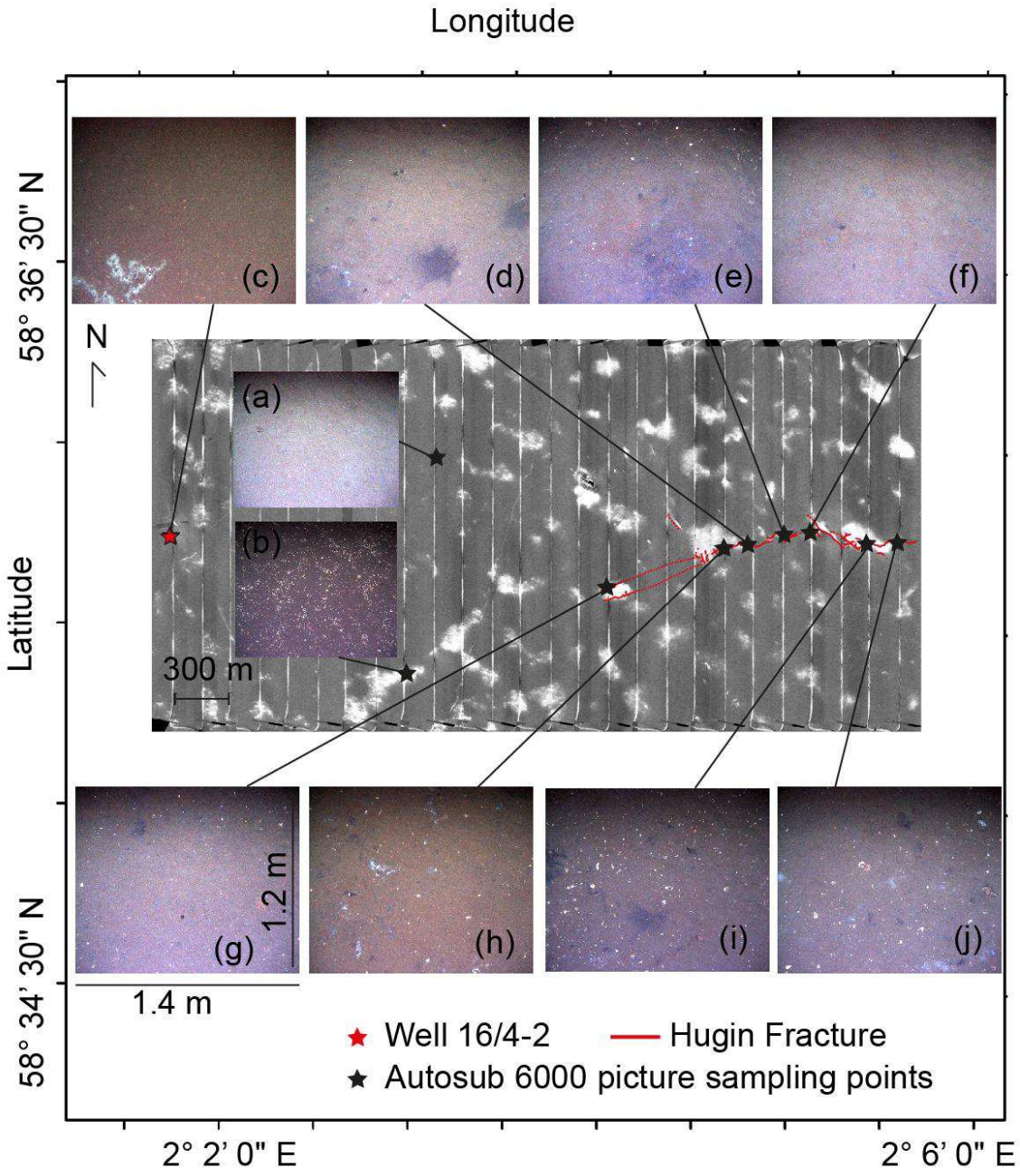
Longitude
58° 36' 30" N
58° 34' 30" N
Latitude
2° 2' 0" E
2° 6' 0" E
N
(a)
(b)
(c)
(d)
(e)
(f)
(g)
(h)
(i)
(j)
300 m
1.2 m
1.4 m
Well 16/4-2
Hugin Fracture
Autosub 6000 picture sampling points

Figure3.

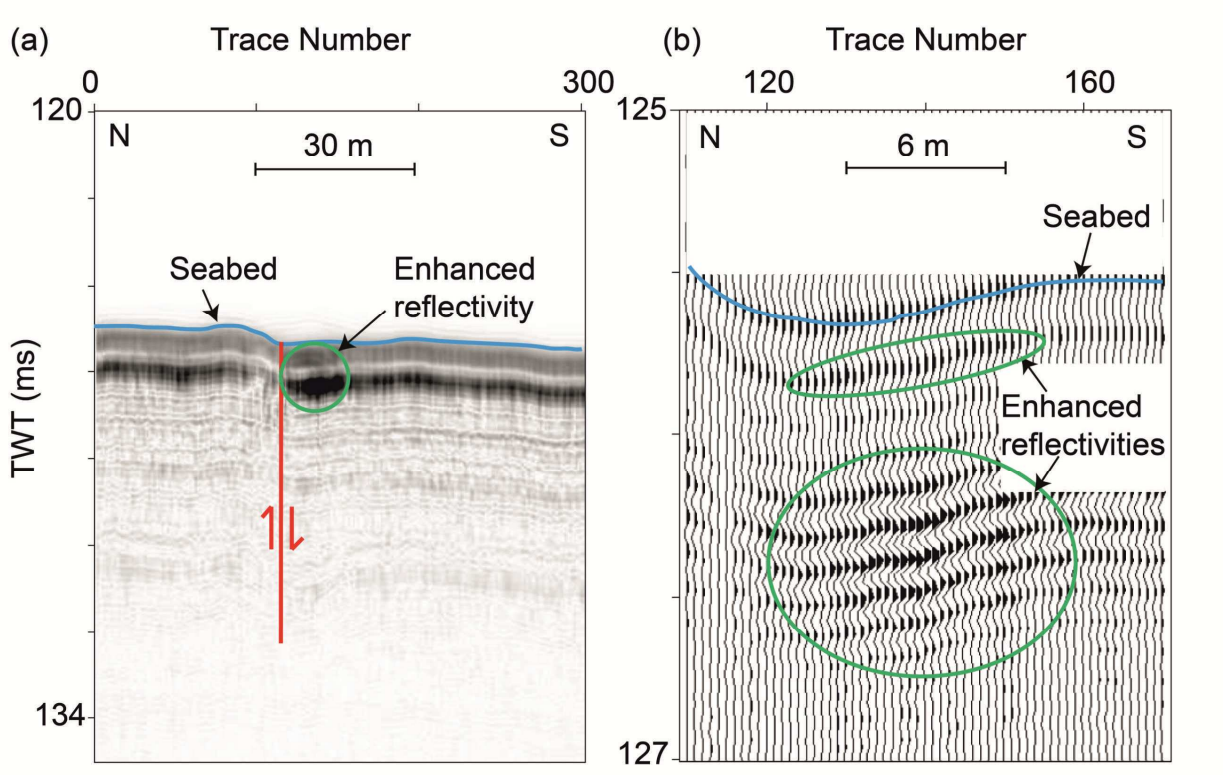
(a)
Trace Number
0
300
120
N
30 m
S
Seabed
Enhanced
reflectivity
TWT (ms)
134
(b)
Trace Number
120
160
125
N
6 m
S
Seabed
Enhanced
reflectivities
127

Figure4.

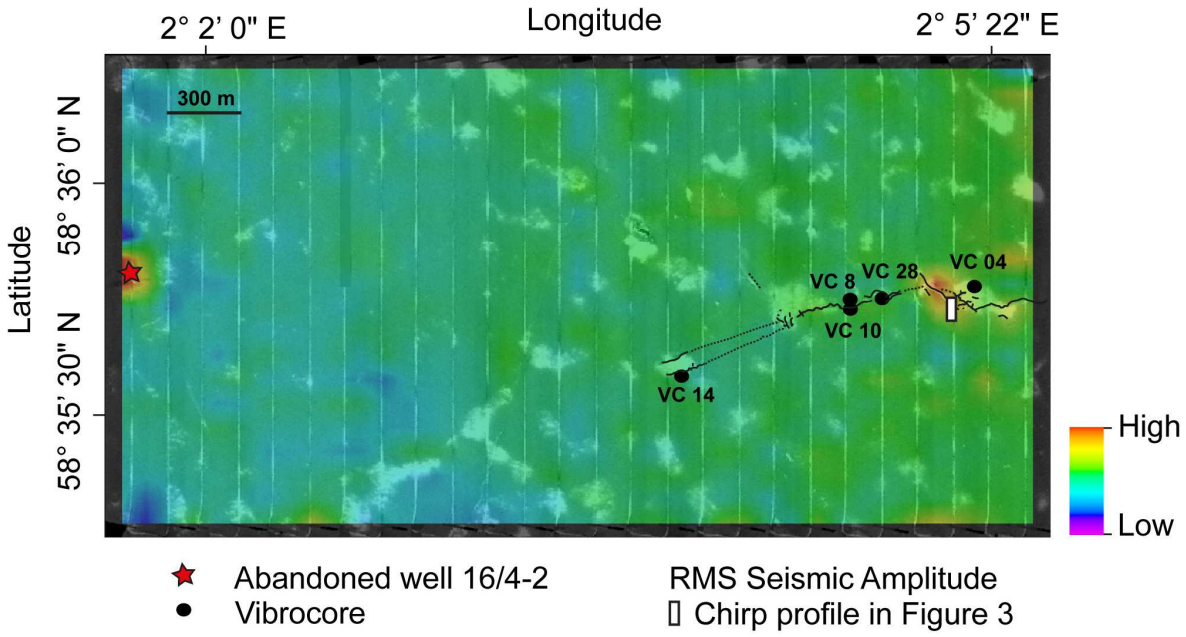
2° 2’ 0" E
Longitude
2° 5’ 22" E
300 m
Latitude
58° 36’ 0" N
58° 35’ 30" N
VC 8
VC 28
VC 04
VC 10
VC 14
High
Low
Abandoned well 16/4-2
Vibrocore
RMS Seismic Amplitude
Chirp profile in Figure 3

Figure5.

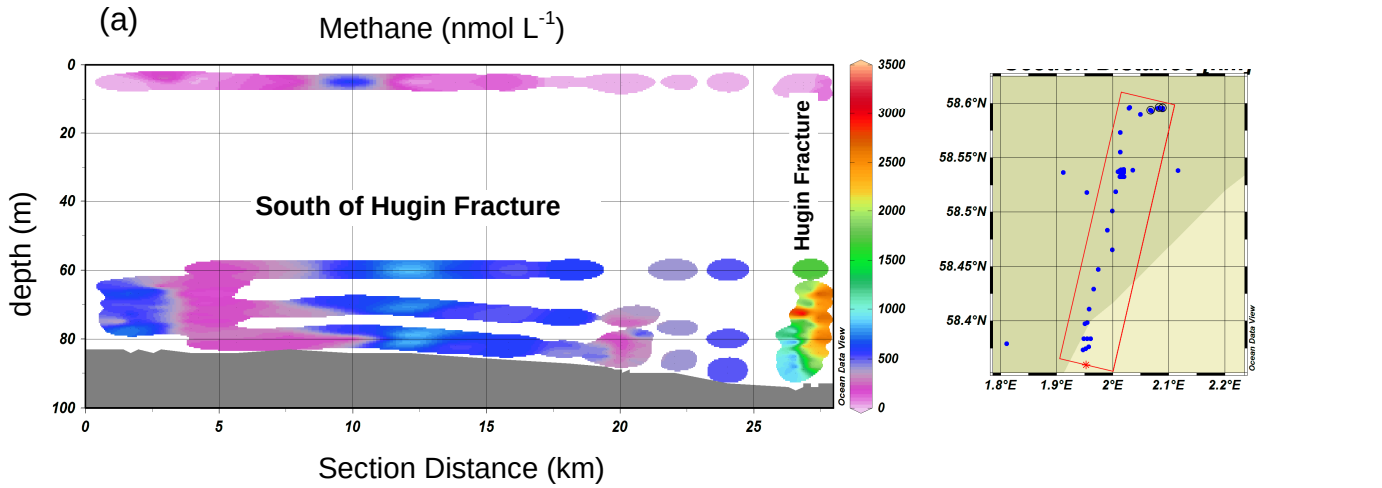
(a)
Methane (nmol L-1)
depth (m)
South of Hugin Fracture
Hugin Fracture
Section Distance (km)
Ocean Data View
58.6°N
58.55°N
58.5°N
58.45°N
58.4°N
1.8°E
1.9°E
2°E
2.1°E
2.2°E

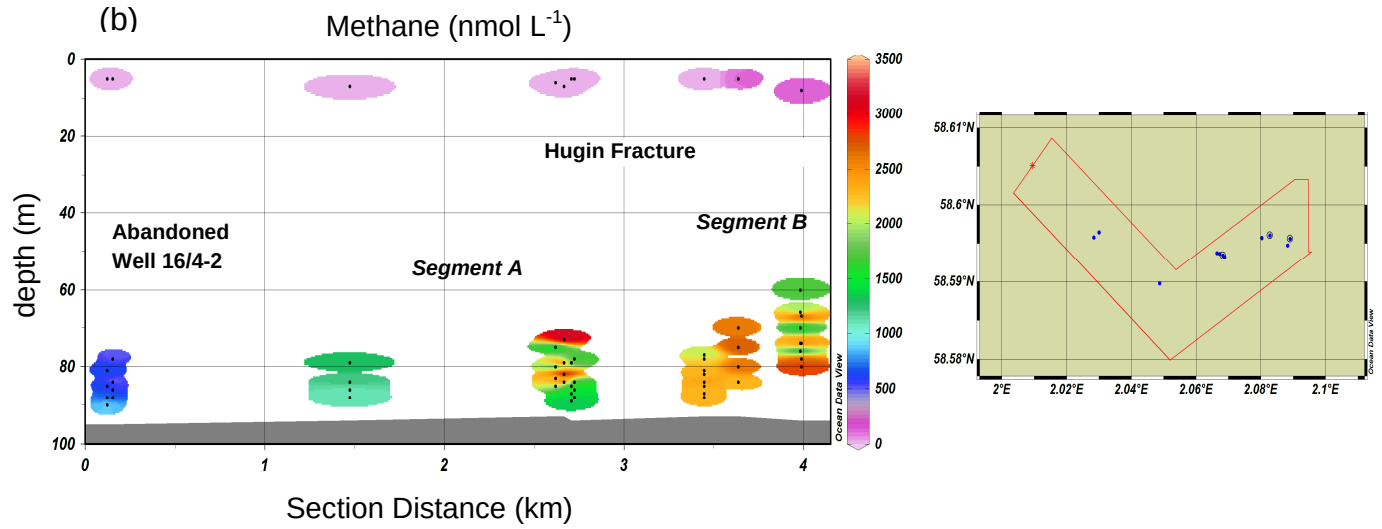
(b)
Methane (nmol L-1)
depth (m)
Hugin Fracture
Abandoned
Well 16/4-2
Segment A
Segment B
Section Distance (km)
Ocean Data View
58.61°N
58.6°N
58.59°N
58.58°N
2°E
2.02°E
2.04°E
2.06°E
2.08°E
2.1°E

Figure6.

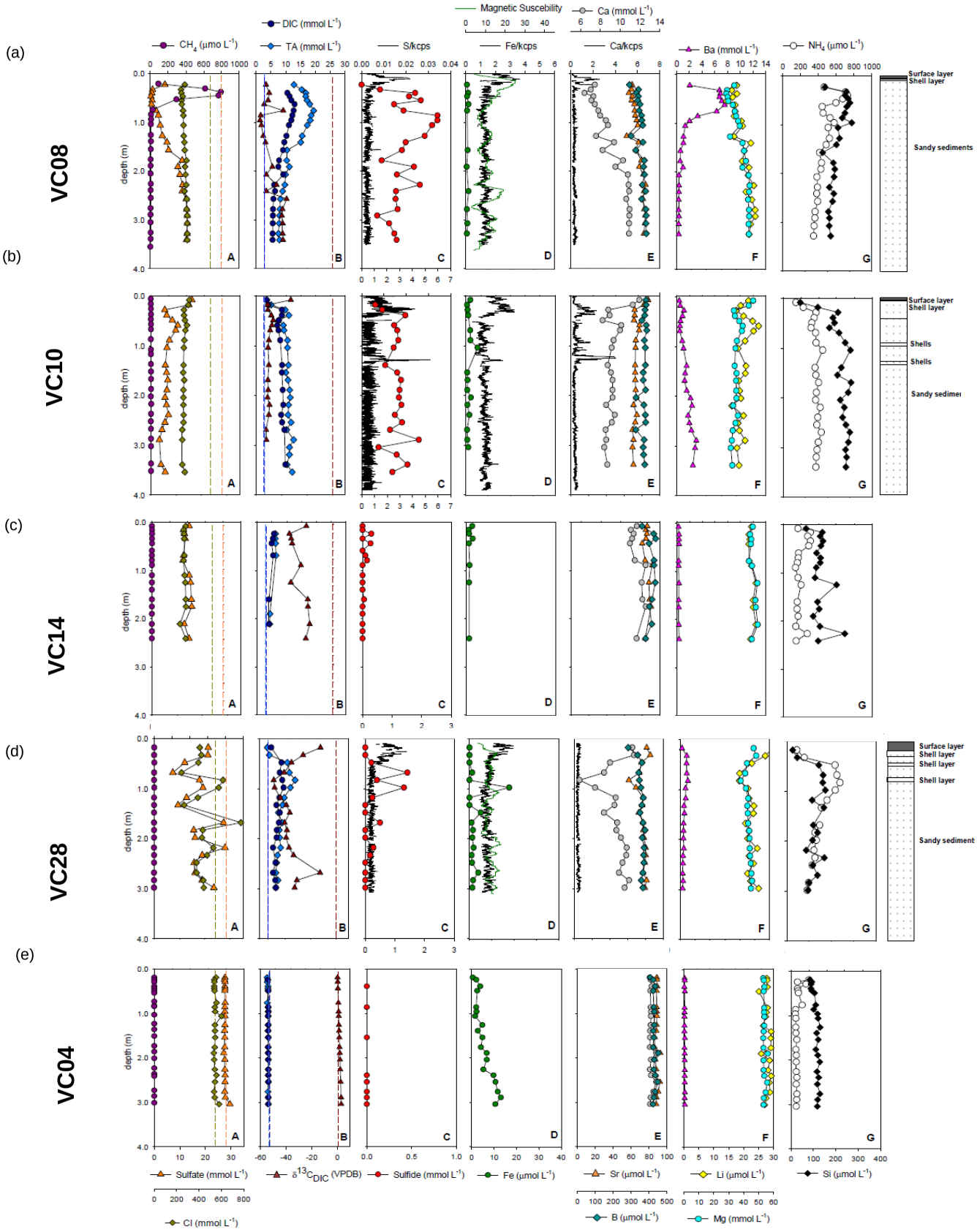
(a)
VC08
(b)
VC10
(c)
VC14
(d)
VC28
(e)
VC04
CH4 (μmo L-1)
DIC (mmol L-1)
TA (mmol L-1)
S/kcps
Magnetic Suscebility
Fe/kcps
Ca (mmol L-1)
Ca/kcps
Ba (mmol L-1)
NH4 (μmo L-1)
depth (m)
A
B
C
D
E
F
G
Surface layer
Shell layer
Sandy sediments
Shells
Sandy sediment
Sulfate (mmol L-1)
δ13CDIC (VPDB)
Sulfide (mmol L-1)
Fe (μmol L-1)
Sr (μmol L-1)
Li (μmol L-1)
Si (μmol L-1)
Cl (mmol L-1)
B (μmol L-1)
Mg (mmol L-1)

Figure7.

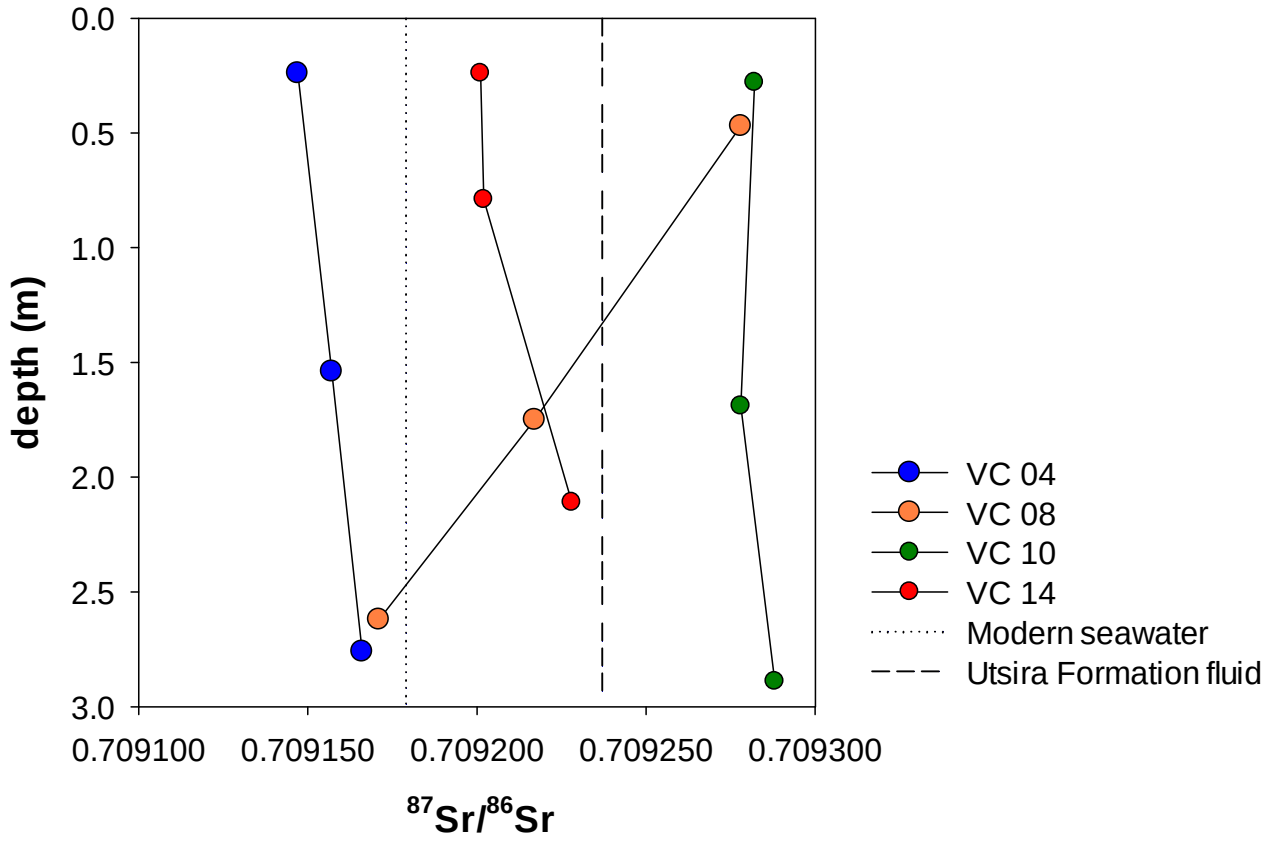
0.0
0.5
1.0
1.5
2.0
2.5
3.0
depth (m)
0.709100
0.709150
0.709200
0.709250
0.709300
87Sr/86Sr
VC 04
VC 08
VC 10
VC 14
Modern seawater
Utsira Formation fluid